CRYSTAL Research&Technology
www.crt-journal.org

Mechanochemical Synthesis of Cesium Titanium Halide Perovskites $Cs_2TiBr_{6-x}I_x$ ($x = 0, 2, 4, 6$)

Christian Kupfer, Jack Elia, Masashi Kato, Andres Osvet, and Christoph J. Brabec*

Perovskite materials have a great variety of applications, such as X-ray detection, lasing and piezoelectric, or solar energy harvesting. While achieving record efficiencies, perovskite solar cells suffer from the presence of toxic lead in their crystal structure. One possibility to circumvent this issue is via the family of vacancy-ordered double-perovskites, where lead atoms are replaced alternatingly by a tetravalent atom and a vacant lattice site. From this material family, Cs_2TiBr_6 has recently emerged as a promising candidate due to its favorable reported properties for photovoltaic applications specifically. This paper presents a novel and facile synthesis route to obtain phase-pure Cs_2TiBr_6 and its lesser-studied iodine-based relatives $Cs_2TiBr_4I_2$, $Cs_2TiBr_2I_4$, and Cs_2TiI_6 via high-energy mechanochemical ball milling. The materials are characterized with structural, microscopic, and photophysical techniques to reveal indirect bandgaps with values of 1.88, 1.13, 1.04, and 1.02 eV but also a distinct lack of any significant photoluminescence (PL) and a high instability under ambient conditions. These findings enable us to clarify the previously controversial properties of Cs_2TiBr_6 and establish its role in the vast landscape of perovskite photovoltaics.

1. Introduction

While perovskite-based solar cells have skyrocketed toward record efficiencies beyond 25% over the course of the last 10 years,[1] two major hurdles still stand in the way of their commercial success: the toxicity of lead, which is commonly found in the champion cells, and their limited stability. Recently, increasing efforts have been made to reduce the amount of lead or replace it altogether.[2] Different strategies to substitute lead have been employed, including homovalent substitution by tin[3] or germanium[4] and heterovalent substitution by a combination of mono- and trivalent atoms, e.g., silver and bismuth[5] or silver and indium.[6] The latter approach, which leads to so-called double-perovskites with the formula $A_2B(I)B(III)X_6$, can be taken even further to produce vacancy-ordered perovskites, a structure where lead is replaced alternatingly by a tetravalent atom and a vacancy in the lattice to maintain charge neutrality.[7] One of the materials in this category, $Cs_2Ti(IV)Br_6$, has recently attracted attention due to its high environmental stability and promising initial power conversion efficiency of 3.3 %.[8] However, there have also been reports questioning some of the reported results and the viability of Cs_2TiBr_6 as an active material for solar cells.[9] In this work, we aim to provide clarity regarding the fundamental properties of Cs_2TiBr_6 and its iodine-based counterparts.

Since the production of a complete device or even of a high-quality thin-film can be a difficult and time-consuming process with multiple optimization steps, we chose a more easily accessible experiment to verify the fundamental material properties. This knowledge can then be used to decide whether it is worth exploring the material further, or if its potential is already limited by those elementary characteristics. Therefore, we report the successful synthesis of phase-pure Cs_2TiBr_6 via facile high-energy mechanochemical ball milling and provide a structural and photophysical characterization of the obtained material. We furthermore show that the same technique can be used to prepare Cs_2TiI_6 as well as the compounds with mixed X-site, which have thus far received less attention, and perform the same characterization.

2. Fundamentals of Mechanochemical Ball Milling Synthesis

Mechanochemical ball milling is a synthesis method that relies on repeated deformation and size reduction of the precursor materials, similar to grinding with mortar and pestle.[10–12] The

C. Kupfer, J. Elia, A. Osvet, C. J. Brabec
Faculty of Engineering, Department of Material Science
Institute Materials for Electronics and Energy Technology (i-MEET)
Friedrich-Alexander-Universität Erlangen-Nürnberg
Martensstraße 7, 91058 Erlangen, Germany
E-mail: christian.kupfer@fau.de
M. Kato
Department of Electrical and Mechanical Engineering
Nagoya Institute of Technology
Nagoya 466–8555, Japan
C. J. Brabec
Forschungszentrum Jülich GmbH
Helmholtz-Institut Erlangen-Nürnberg for Renewable Energy (HI ERN)
Immerwahrstraße 2, 91058 Erlangen, Germany

The ORCID identification number(s) for the author(s) of this article can be found under https://doi.org/10.1002/crat.202200150

DOI: 10.1002/crat.202200150

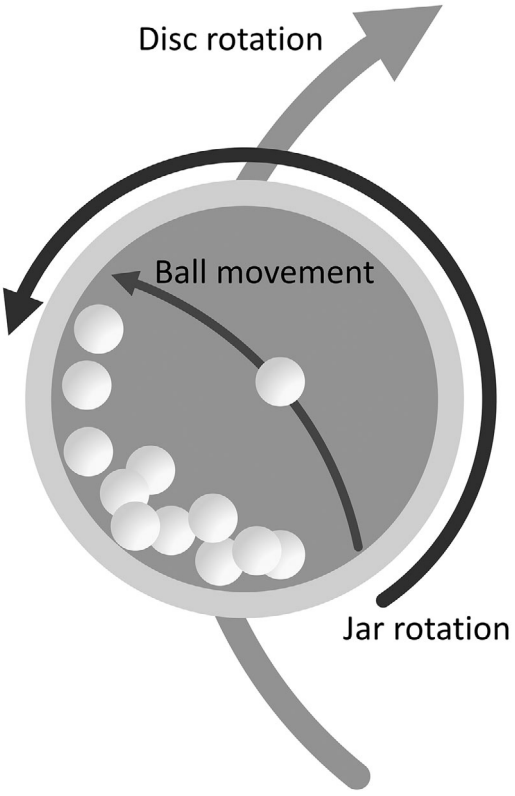

Figure 1. Schematic of the ball milling process.

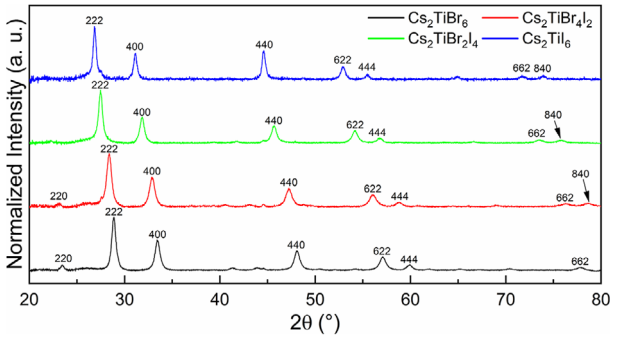

Figure 2. X-ray diffraction patterns of cesium-titanium halides obtained by mechanochemical ball milling for 17 h at 235 RPM: Cs_2TiBr_6 (black), $Cs_2TiBr_4I_2$ (red), $Cs_2TiBr_2I_4$ (green), and Cs_2TiI_6 (blue). The shift of the pattern indicates a unit-cell expansion for compounds containing iodine. The most prominent peaks are labeled with their respective Miller-indices, a full list of identified peaks can be found in Table 1.

precursors are loaded into a dedicated crucible with the desired stoichiometry alongside the milling balls. The crucible is then sealed and mounted on the disc of a planetary ball mill, which enables the simultaneous rotation of the jar around its own central axis and the center of the disc at an adjustable rotation frequency. This motion leads to a repeated detaching of the milling balls from the wall of the crucible followed by an impact on other balls or the precursor powders, causing the particles to deform and rupture in the process. This simultaneously leads to a reduction of the precursor particle size, an increase of the surface area and to homogenous mixing while providing the energy necessary for the reaction. After the milling is finished, the resulting powder can simply be extracted from the jar and sieved to avoid large agglomerates. This process is schematically shown in **Figure 1**. In the past, this synthesis method has been successfully employed to produce high-quality perovskite powders of materials such as $MAPbI_3$,[13] $Cs_2AgBiBr_6$, $MA_2TlBiBr_6$, and $Cs_2AgSbBr_6$.[14]

Compared to other synthesis methods, mechanochemical ball milling poses many advantages such as the ease of upscaling and the nonreliance on the solubility of the precursors, which in turn leads to a larger available pool of possible reactants.[13] Furthermore, because there is no necessity for a solvent, ball milling is inherently a "green" process. This also eliminates the risk of incomplete solvent removal from the material after the synthesis procedure. However, there is the danger of contamination of the powder with abrasion from the crucible or milling balls and an increase in crystal defect density due to the high mechanical forces.[11]

3. Results

In previous reports, vapor-solid reactions[8] and solution processing[9,15–17] have been successfully employed to synthesize Cs_2TiBr_6. In this work, we report a novel, mechanochemical synthesis approach using high-energy ball milling to obtain phase-pure $Cs_2TiBr_{6-x}I_x$ ($x = 0, 2, 4, 6$) powders. Both synthesis and characterization are performed in a nitrogen atmosphere (either in the glovebox or with proper encapsulation) to avoid the fast degradation that occurs upon exposure of the materials to the ambient atmosphere.

3.1. Powder X-Ray Diffraction Measurements

The XRD (X-ray diffraction) patterns of Cs_2TiBr_6 and the related iodine compounds are shown in **Figure 2**. Upon incorporation of increasing amounts of iodine into the lattice, the XRD peaks shift continuously toward lower angles, indicating a slight expansion of the crystal lattice. The Kapton tape, which is used to protect the sample from environmental stress and degradation during the measurement procedure, produces an additional amorphous background at lower angles, which was accounted for during analysis.

The XRD pattern of Cs_2TiBr_6 is consistent with the one obtained by Kozhina and Korol'kov,[18] and no peaks of the precursor materials remain, indicating a complete conversion to the desired reaction products. Similarly, the pattern of Cs_2TiI_6 matches the reports from the corresponding literature.[19] A full list of identified peaks with their respective Miller-indices and peak positions is given in **Table 1**. Additionally, the reference values of the peak positions for Cs_2TiBr_6 and Cs_2TiI_6 from literature are included. The good agreement between the measured and previously reported values is indicative of a successful synthesis, and the absence of additional peaks confirms the phase purity of the obtained materials.

From the powder X-ray diffraction measurements, the unit cell parameters of the different materials can be determined. This analysis was performed with the software described by Holland and Redfern.[20] The results show that all materials exhibit a cubic crystal structure with lattice parameters of 10.70 Å

Table 1. XRD peak positions and corresponding Miller-indices for $Cs_2TiBr_{6-x}I_x$ ($x = 0, 2, 4, 6$) determined experimentally and the corresponding literature values for Cs_2TiBr_6 and Cs_2TiI_6 in comparison.

Miller indices			Experimental peak position 2θ [°]				Peak position from literature 2θ [°]	
h	*k*	*l*	Cs_2TiBr_6	$Cs_2TiBr_4I_2$	$Cs_2TiBr_2I_4$	Cs_2TiI_6	Cs_2TiBr_6[18]	Cs_2TiI_6[19]
2	2	0	23.45	23.08	/	/	23.75	21.89
2	2	2	28.85	28.35	27.45	26.85	29.19	26.90
4	0	0	33.44	32.87	31.82	31.11	33.91	31.16
4	2	2	41.31	40.46	/	/	41.75	38.41
5	1	1	43.90	43.10	41.69	/	44.41	40.84
4	4	0	48.06	47.22	45.66	44.58	48.59	44.64
5	3	1	50.40	/	/	/	50.98	46.81
6	2	0	54.16	/	/	/	54.78	50.25
6	2	2	57.05	56.02	54.13	52.88	57.70	52.89
4	4	4	59.85	58.77	56.74	55.44	60.52	55.44
7	1	1	61.88	/	/	/	62.59	57.45
6	4	2	65.16	/	/	/	65.96	60.32
7	3	1	67.18	/	/	/	67.93	62.09
8	0	0	70.33	68.97	66.52	64.84	71.17	64.98
6	6	2	77.75	76.21	73.45	71.67	78.71	71.65
8	4	0	/	78.58	75.72	73.89	81.17	73.81

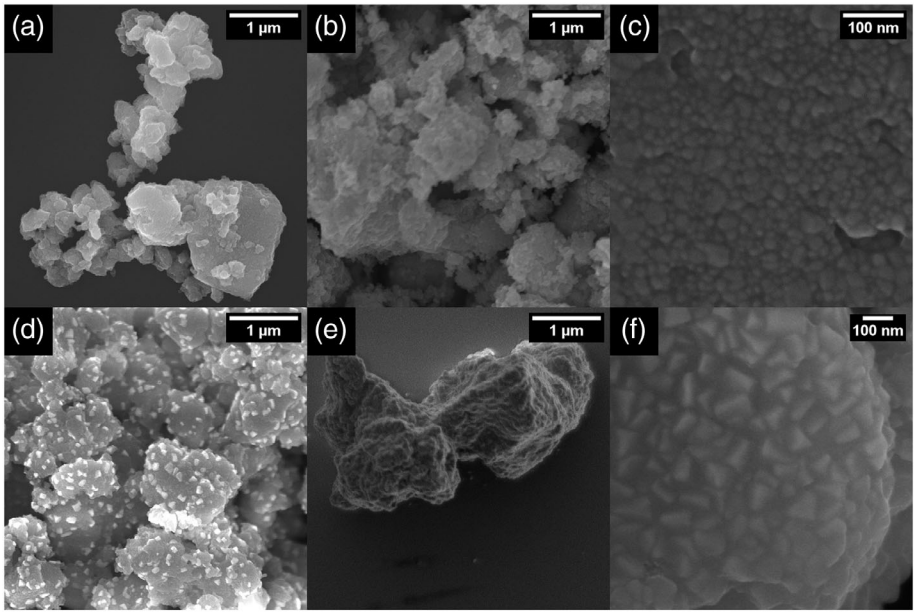

Figure 3. Scanning electron microscopy images of a) Cs_2TiBr_6 particles, b) $Cs_2TiBr_2I_4$ particles, c) Cs_2TiBr_6 particle surface with increased magnification and visible crystallites, d) $Cs_2TiBr_4I_2$ particles with bright flakes on the surfaces, originating from degradation due to exposure to ambient moisture, e) Cs_2TiI_6 particle, and f) Cs_2TiI_6 particle surface with increased magnification and visible white flakes.

(Cs_2TiBr_6), 10.88 Å ($Cs_2TiBr_4I_2$), 11.23 Å ($Cs_2TiBr_2I_4$), and 11.48 Å (Cs_2TiI_6).

3.2. Scanning Electron Microscopy

Scanning electron microscopy (SEM) images of the freshly synthesized cesium-titanium halide powders were taken after drop-casting them onto silicon substrates from a hexane dispersion. The obtained pictures are shown in **Figure 3**.

The SEM images of Cs_2TiBr_6 (see Figure 3a) show particle sizes of the mechanochemically synthesized powder in the order of a few micrometers. With enhanced magnification, a finer structure becomes visible in Cs_2TiBr_6, showing the individual crystallites comprising the particles (see Figure 3c). These crystallites manifest in sizes of a few to tens of nanometers. In contrast

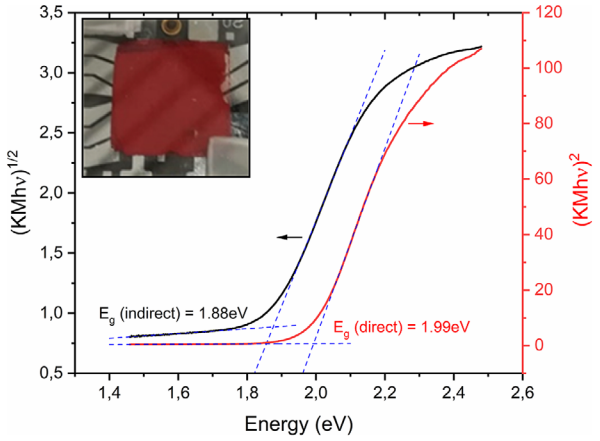

Figure 4. Kubelka-Munk plot of the measured reflectance spectra of Cs_2TiBr_6 to determine the indirect (left axis, black curve) and direct (right axis, red curve) bandgaps. Dashed blue lines are fits to the linear regimes of the spectra and the background. The bandgaps are found by calculating the intercept of the two linear regressions. Inset: Photograph of a film produced by drop-casting the material dispersed in hexane onto a glass substrate with finger contacts.

to the pictures of Cs_2TiBr_6, the image of $Cs_2TiBr_4I_2$ (see Figure 3d) shows bright spots on the surface of the individual particles. These spots appear because of electrical charging of the material under the influence of the electron beam in the SEM. The origin of this is a build-up of electrons in regions with reduced conductivity. We believe that this stems from degradation of the material during the transfer to the SEM chamber, resulting in isolating CsI appearing on the surface. This hypothesis is supported by visual observations of the film, showing a change in color from black to slightly yellowish in areas where a large density of bright flakes was apparent under the SEM. A similar but less pronounced phenomenon can be observed on Cs_2TiI_6 upon enhancing the magnification (see Figure 3f).

3.3. Photophysical Characterization

The optical properties of the materials were first investigated by UV-Vis measurements. The reflectance spectra are plotted according to the Kubelka-Munk (KM) theory[21] for both the assumption of a direct and an indirect allowed transition (see **Figure 4**).

The respective bandgaps are then extracted by determining the intercept of the linear regime in the KM plot with the background according to the Tauc-formalism.[22] The bandgap value of Cs_2TiBr_6 is 1.99 eV for direct transitions and 1.88 eV for indirect transitions, establishing Cs_2TiBr_6 as an indirect semiconductor. These experimentally determined values are consistent with those recently extracted by Euvrard et al.[9] (2.0 and 1.9 eV, respectively), but contradict the previously reported direct bandgap of 1.8 eV.[8] Both direct and indirect bandgaps decrease rapidly once bromine is partially replaced by iodine in the lattice, leading to significantly reduced bandgap values of 1.22, 1.14, and 1.10 eV for direct allowed transitions and 1.13, 1.04, and 1.02 eV for indirect allowed transitions in $Cs_2TiBr_4I_2$, $Cs_2TiBr_2I_4$, and Cs_2TiI_6 respectively. The evolution of the different bandgaps with iodine content in $Cs_2TiBr_{6-x}I_x$ ($x = 0, 2, 4, 6$) is shown in **Figure 5**a.

DFT calculations performed by other groups[8,9] predict a direct bandgap that is 30 meV larger than the value for the indirect transition, making Cs_2TiBr_6 a quasi-direct semiconductor. Our experiments reveal a slightly larger difference between the fundamental direct and indirect bandgaps of this material class (see Figure 5b).

Additionally, we attempted to measure PL spectra and transients with a Fluotime300 steady-state and lifetime spectrometer (PicoQuant) with a 402 nm pump laser, but no significant luminescence signal could be detected. The lack of luminescence is consistent with the indirect nature of the bandgap and with the observations of Euvrard et al.,[9] who report an extremely weak PL peak centered around 1.75 eV.

3.4. Stability

When considering candidate materials for potential solar applications, not only photophysical and performance properties are important, but considerable thought must be attributed to the stability of the material. In recent reports, conflicting results have been presented regarding the environmental stability of Cs_2TiBr_6 and its related iodine compounds. While Chen et al.[8] present Cs_2TiBr_6-based solar cells unfazed by air, moisture, and

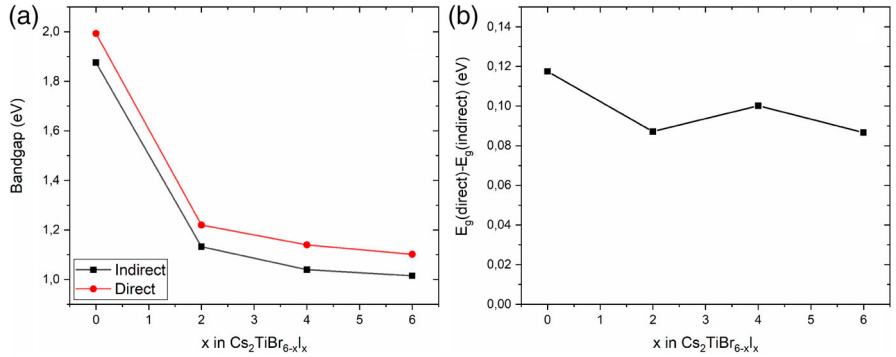

Figure 5. a) Evolution of direct (red) and indirect (black) bandgaps for different material compositions, determined according to the KM theory. While the pure bromide compound shows a large bandgap, it gets drastically reduced once iodine is incorporated into the crystal structure. b) Difference between direct and indirect bandgap value of the different material compositions. The bandgaps of all investigated compounds are strictly indirect in nature.

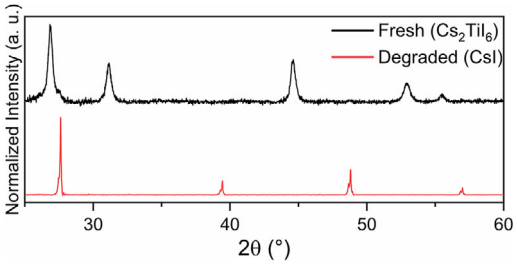

Figure 6. Comparison of the XRD patterns of freshly prepared Cs_2TiI_6 (black) and the same powder after degradation to CsI (red).

heat-related stress for at least 20 h, other reports[9,17] found the material to be quickly degrading upon removal from inert nitrogen atmosphere. The latter observation is in line with our findings of a material that is stable when handled in nitrogen but rapidly degrades in a matter of minutes when exposed to ambient conditions, turning from its original crimson red color to a lighter orange and subsequently to almost completely white. The remaining white powder can be identified as CsBr or CsI via XRD measurements (see **Figure 6**). While the increased surface area of a loose powder in comparison to a film will certainly accelerate the degradation of the material, its swift decomposition is still a considerable challenge on the road to commercialization. Furthermore, the instability issue is increasingly amplified the more iodine is incorporated in place of bromine, fostering even faster decomposition.

4. Conclusion

In this work, we have presented a novel synthesis procedure for producing high-purity $Cs_2TiBr_{6-x}I_x$ ($x = 0, 2, 4, 6$) powders, using high-energy ball milling. Structural investigation and unit cell characterization of the materials was conducted via XRD measurements, revealing a high phase purity. Furthermore, UV-Vis spectroscopy measurements in reflectance geometry have been performed to determine the direct and indirect bandgaps of the powders. All materials of the $Cs_2TiBr_{6-x}I_x$ family manifest as indirect semiconductors with bandgaps of 1.88, 1.13, 1.04, and 1.02 eV for $x = 0, 2, 4, 6$, respectively, with direct bandgaps roughly 0.1 eV larger. While the experimentally determined bandgaps are certainly appropriate for tandem or single-junction photovoltaic applications, their indirect nature is quite disadvantageous. Additionally, the high instability is undoubtedly a greatly limiting factor for a successful cesium titanium halide solar cell.

5. Experimental Section

Synthesis: Cs_2TiBr_6 was synthesized via mechanochemical ball milling as described in the previous chapter. The precursors, CsBr and $TiBr_4$, were loaded into a 45 ml agate crucible inside a nitrogen-filled glovebox with a 10 % excess of $TiBr_4$ over the stoichiometric amount due to the high volatility of this compound. Yttrium-stabilized ZrO_2 milling balls with 10 mm diameter were added, the crucible was closed, and the lid sealed with self-sealing thermoplastic (parafilm). The milling was performed in a planetary ball mill and the milling time, the number of milling balls, and the rotations per minute were adjusted to provide optimal results. Pure Cs_2TiBr_6 was obtained after 17 h of constant milling with five milling balls at 235 RPM. Additionally, experiments with higher rotation speed yielded equally good results with just 5 h of milling, with 15 min breaks every full hour, using 10 milling balls at 550 RPM. The underlying chemical reaction and example weights of the precursors are given in Equation (1).

$$2CsBr(815mg) + TiBr_4(794mg) \rightarrow Cs_2TiBr_6 \quad (1)$$

Furthermore, compounds with mixed iodine/bromine X-sites as well as purely iodine-based materials were also successfully produced, following the same routine as mentioned above but with CsI in place of CsBr and/or TiI_4 replacing $TiBr_4$. It should be noted that using the stoichiometric amount of TiI_4 is sufficient, and no excess material needs to be added to ensure proper synthesis results. The reactions for obtaining pure and mixed iodine compounds are given in Equations (2)–(4).

$$2CsI + TiBr_4 \rightarrow Cs_2TiBr_4I_2 \quad (2)$$

$$2CsBr + TiI_4 \rightarrow Cs_2TiBr_2I_4 \quad (3)$$

$$2CsI + TiI_4 \rightarrow Cs_2TiI_6 \quad (4)$$

Characterization: X-ray diffraction patterns were recorded with a Panalytical Empyrean Series 2 X-ray diffractometer using Cu-Kα radiation from an X-ray source, operating at 40 kV and 30 mA. The sample holder for the XRD measurements was loaded with freshly produced powder in an inert nitrogen atmosphere and subsequently covered with Kapton-tape to avoid exposing the sample to ambient atmosphere before or during the measurement.

UV-Vis measurements were performed with a PerkinElmer Lambda 950 UV/VIS Spectrometer in reflectance geometry with the sample at the backside of an integrating sphere. The recorded reflectance spectra with a step width of 1 nm and an integration time of 1s were analyzed according to the Kubelka-Munk theory, and the direct and indirect bandgaps were determined by the intersect of the linear part of the KM plot with the background.

High-resolution SEM images were obtained using a Jeol JSM-7610F Schottky field emission scanning electron microscope (Japan) at 15 kV acceleration voltage. The SEM samples were prepared by dispersing the freshly milled powders in hexane and drop-casting a small amount of this dispersion onto silicon substrates. After drying in nitrogen atmosphere, the samples were transported to the SEM in a sealed tube from which they were quickly inserted into the SEM, where a vacuum was drawn, therefore, the time exposed to ambient atmosphere was minimized to avoid degradation of the sample.

Acknowledgements

The authors gratefully acknowledge financial support for this work by the Deutsche Forschungsgemeinschaft under GRK 2495/E.

Open Access funding enabled and organized by Projekt DEAL.

Conflict of Interest

The authors declare no conflict of interest.

Data Availability Statement

The data that support the findings in this study are available from the corresponding author upon reasonable request.

Keywords

ball milling, cesium titanium halides, lead-free, stability

Received: June 30, 2022
Revised: September 27, 2022
Published online: November 15, 2022

[1] NREL. https://www.nrel.gov/pv/cell-efficiency.html **2021**.
[2] F. Giustino, H. J. Snaith, *ACS Energy Lett.* **2016**, *1*, 1233.
[3] W. Ke, C. C. Stoumpos, M. G. Kanatzidis, *Adv. Mater.* **2019**, *31*, 1803230.
[4] R. Chiara, M. Morana, L. Malavasi, *Chempluschem* **2021**, *86*, 879.
[5] W. Gao, C. Ran, J. Xi, J. Bo, W. Zhang, M. Wu, X. Hou, Z. Wu, *ChemPhysChem* **2018**, *19*, 1696.
[6] G. Volonakis, A. A. Haghighirad, R. L. Milot, W. H. Sio, M. R. Filip, B. Wenger, M. B. Johnston, L. M. Herz, H. J. Snaith, F. Giustino, *J. Phys. Chem. Lett.* **2017**, *8*, 772.
[7] A. E. Maughan, A. M. Ganose, D. O. Scanlon, J. R. Neilson, *Chem. Mater.* **2019**, *31*, 1184.
[8] M. Chen, M.-G. Ju, A. D. Carl, Y. Zong, R. L. Grimm, J. Gu, Z. Cheng, Y. Zhou, N. Padture, *Joule* **2018**, *2*, 558.
[9] J. Euvrard, X. Wang, T. Li, Y. Yan, D. B. Mitzi, *J. Mater. Chem. A* **2020**, *8*, 4049.
[10] A. Stolle, T. Szuppa, S. E. S. Leonhardt, B. Ondruschka, *Chem. Soc. Rev.* **2011**, *40*, 2317.
[11] C. C. Koch, *Nanostruct. Mater.* **1997**, *9*, 13.
[12] P. Dulian, Perovskite Materials - Synthesis, Characterisation, Properties, and Applications, InTech, USA **2016**.
[13] N. Leupold, K. Schötz, S. Cacovich, I. Bauer, M. Schultz, M. Daubinger, L. Kaiser, A. Rebai, J. Rousset, A. Köhler, P. Schulz, R. Moos, F. Panzer, *ACS Appl. Mater. Interfaces* **2019**, *11*, 30259.
[14] G. García-Espejo, D. Rodríguez-Padrón, R. Luque, L. Camacho, G. De Miguel, *Nanoscale* **2019**, *11*, 16650.
[15] D. Kong, D. Cheng, X. Wang, K. Zhang, H. Wang, K. Liu, H. Li, X. Sheng, L. Yin, *J. Mater. Chem. C* **2020**, *8*, 1591.
[16] G. Grandhi, A. Matuhina, M. Liu, S. Annurakshita, H. Ali-Löytty, G. Bautista, P. Vivo, *Nanomaterials* **2021**, *11*, 1458.
[17] S. M. Liga, G. Konstantatos, *J. Mater. Chem. C* **2021**, *9*, 11098.
[18] D. V. Korol'kov, I. I. Kozhina, *Transl. Zh. Strukt. Khim.* **1965**, *6*, 84.
[19] D. Sinram, C. Brendel, B. Krebs, *Inorg. Chim. Acta* **1982**, *64*, L131.
[20] T. J. B. Holland, S. A. T. Redfern, *Mineral. Mag.* **1997**, *61*, 65.
[21] P. Kubelka, F. Munk, *Z. Tech. Phys.* **1931**, *12*, 593.
[22] J. Tauc, R. Grigorovici, A. Vancu, *Phys. Status Solidi* **1966**, *15*, 627.